West African Monsoon Intraseasonal Variability: A Precipitable Water Perspective

D. EMMANUEL POAN, ROMAIN ROEHRIG, FLEUR COUVREUX, AND JEAN-PHILIPPE LAFORE

CNRM-GAME, Météo France, and CNRS, Toulouse, France

(Manuscript received 12 March 2012, in final form 17 October 2012)

ABSTRACT

West African monsoon intraseasonal variability has important implications for food security and drought early warnings. In the present study, intraseasonal variability over the Sahel is assessed from the perspective of precipitable water, as provided by model reanalyses and GPS measurements. In the eastern Sahel, precipitable water variability is dominated by time scales longer than 10 days, whereas synoptic scales dominate in the western Sahel, especially because of African easterly waves (AEWs).

The present work then focuses on the moisture footprint of AEWs along the northern side of the African easterly jet, as detected and analyzed directly from the main synoptic disturbances associated with precipitable water. Composite wet and dry precipitable water anomalies within AEWs propagate westward with a 5–6-day period. Their robustness, consistency, and spatial footprint, as well as their significant modulation of the convective activity, imply potential skill for short- to medium-range forecasts of wet and dry events over the Sahel. A composite moisture budget points out the key processes involved in the evolution of moisture anomalies. Advection processes are shown to be dominant during their life cycle. A linear adiabatic analysis of the propagation and growth of AEW precipitable water anomalies captures the main observed properties well, even though a key role of diabatic processes such as rain evaporation is needed to fully understand the life cycle of such precipitable water anomalies, especially their growth over the continent.

1. Introduction

Over the Sahel, the monsoon brings most of the rainfall during a 3–4-month period, from June to September. This rainy season is punctuated by dry and wet periods occurring at various intraseasonal time scales (Janicot et al. 2011), which can be dramatic for local populations and economies (Sultan et al. 2005). During the last decade, considerable endeavors have been made to better document and understand the intraseasonal variability[1] (ISV). Three preferred time scales have been highlighted: around 40 days, probably involving the Madden–Julian oscillation (Matthews 2004; Janicot et al. 2009); approximately 15 days with two main regional modes (Mounier and Janicot 2004; Mounier et al. 2008; Janicot et al. 2010; Roehrig et al. 2011); and in the 3–10-day range with the well-known African easterly waves (AEWs; e.g., Reed et al. 1977; Thorncroft and Hoskins 1994; Fink and Reiner 2003; Kiladis et al. 2006; Cornforth et al. 2009; among many others).

Despite this relatively long history of research, fundamental gaps remain in the understanding of the West African monsoon ISV, especially with regard to the interaction between the dynamics and the convection within intraseasonal disturbances, especially within AEWs. This is partly because precipitation occurs when numerous large- and small-scale conditions are satisfied (e.g., conditional convective instability, availability of water and energy in the boundary layer, a moist free troposphere, small low-level inhibition, and wind shear). Precipitation and associated variables are therefore often too complex to derive directly a comprehensive understanding of its high spatial and temporal variability, both in observations and numerical models. In the present analysis, we advocate the use of intermediate variables, which can link dynamics and convection, whose evolution can be more easily understood, and which have a crucial role in convective activity.

The moisture field and the derived precipitable water (PW; i.e., the vertically integrated specific humidity) can

[1] In the present study, the ISV refers to time scales from 1 to 90 days (~3 months), and thus includes the synoptic range.

Corresponding author address: D. Emmanuel Poan, CNRM-GAME, Météo France and CNRS, 42 avenue Gaspard Coriolis, 31057 Toulouse, France.
E-mail: emmanuel.poan@meteo.fr

DOI: 10.1175/JAS-D-12-087.1

be seen as such intermediate variables. Observational studies have shown that deep moist convection in the tropics is sensitive to both lower- and free-tropospheric moisture. Increased lower-tropospheric moisture tends to lead to deep convection and precipitation (e.g., Sherwood 1999; Zelinka and Hartmann 2009; Mapes et al. 2009), while high free-tropospheric water vapor tends to provide favorable conditions for the development of deep convection (e.g., Brown and Zhang 1997; Parsons et al. 2000; Redelsperger et al. 2002; Bretherton et al. 2004; Sherwood et al. 2004). More recently, precipitation on daily to monthly and subseasonal time scales has been found to be a nonlinear function of PW, involving some threshold value near which a sharp increase in precipitation occurs (Neelin et al. 2009). Holloway and Neelin (2010) extend these results and emphasize that, though PW increases before precipitation events on both a synoptic time scale and a time scale consistent with mesoscale convective activity, precipitation occurs stochastically during the following 10–12 h. Most of these studies focus on tropical oceans or small tropical islands. Although one might expect some similar critical relationships between PW and precipitation over continental regions, the time and space scales at which such a relationship can appear are less obvious. However, high PW values are presumably a necessary condition for the occurrence of deep convection, and PW is, a priori, simpler, less intermittent, and better captured by general circulation models (e.g., Bock et al. 2008) than precipitation. The documentation of the PW subseasonal variability and its relationship with deep convection can also provide some helpful guidance on the issue of precipitation forecasts over tropical areas. In the following, we propose to analyze the PW synoptic-to-intraseasonal variability over West Africa and relate it to that of precipitation.

Only a few studies have tackled the variability of PW over West Africa, and have done so mainly at the synoptic time scale. Cadet and Houston (1984) identified peaks in the PW variance near 3–4 and 6–9 days. Investigating the water vapor flux over West Africa, especially the contribution of the lower levels, Cadet and Nnoli (1987) also found variability at 3–5 and 5–7 days near 12°N. More recently, Couvreux et al. (2010) showed the existence of intermittent and intense northward penetrations of the monsoon flow (monsoon burst) during the preonset period, with periodicities ranging between 3 and 5 days. Some of these northward excursions of humidity were zonally stationary and related to the Saharan heat low activity, whereas others propagated westward simultaneously with AEWs. The PW synoptic variability could thus be partly attributed to AEWs or to the Saharan heat low activity. Conversely, PW fluctuations may influence AEW dynamics through convective activity, and exert a negative feedback on the heat low as suggested by Couvreux et al. (2010).

The objectives of the present work are (i) to document the regional ISV of PW and (ii) to focus on the synoptic-scale variability through the detection and analysis of the main associated disturbances, their characteristics, and links with convection. Datasets and methods used in this study are briefly described in section 2. Section 3 investigates general features of PW ISV. Section 4 provides a composite analysis of the PW synoptic variability, which will highlight a moisture perspective of AEWs along the northern side of the African easterly jet. Mechanisms at play are discussed in section 5, using an integral moisture budget. Through a linear and adiabatic analysis, section 6 proposes an interpretation of the propagation and growth of the PW anomalies associated with AEWs. Section 7 summarizes our main results and indicates some prospects for future work.

2. Datasets and methods

a. Datasets

A large part of the present study was based on the last European Centre for Medium-Range Weather Forecasts (ECMWF) Interim Re-Analysis (ERA-Interim; Simmons et al. 2007), which uses the 31r1/2 cycle of the ECWMF Integrated Forecast System (IFS). The spectral truncature reaches T799, and the model comprises 91 vertical levels. The 6-hourly (0000, 0600, 1200, and 1800 UTC) reanalysis covers 1989–2007. It is available with a $0.75° \times 0.75°$ horizontal resolution and is vertically sampled on 31 levels.

The daily National Centers for Environmental Prediction (NCEP)–Department of Energy (DOE) Atmospheric Model Intercomparison Project (AMIP-II) reanalysis (NCEP2; Kanamitsu et al. 2002) at a $2.5° \times 2.5°$ horizontal resolution was also used for comparison with the ERA-Interim dataset. The PW quality of these two reanalyses was assessed against independent PW global positioning system (GPS) ground-based observations over West Africa by Bock et al. (2008), and ERA-Interim was shown to perform best for time scales longer than 2 days. These GPS measurements (Bock et al. 2008) were not assimilated in the reanalysis and thus provided independent data to further validate our results.

Daily-averaged outgoing longwave radiation (OLR) data provided by the National Oceanic and Atmospheric Administration (NOAA) polar-orbiting satellites (Liebmann and Smith 1996) was used as a proxy for convective activity. It covered the period from 1979 to

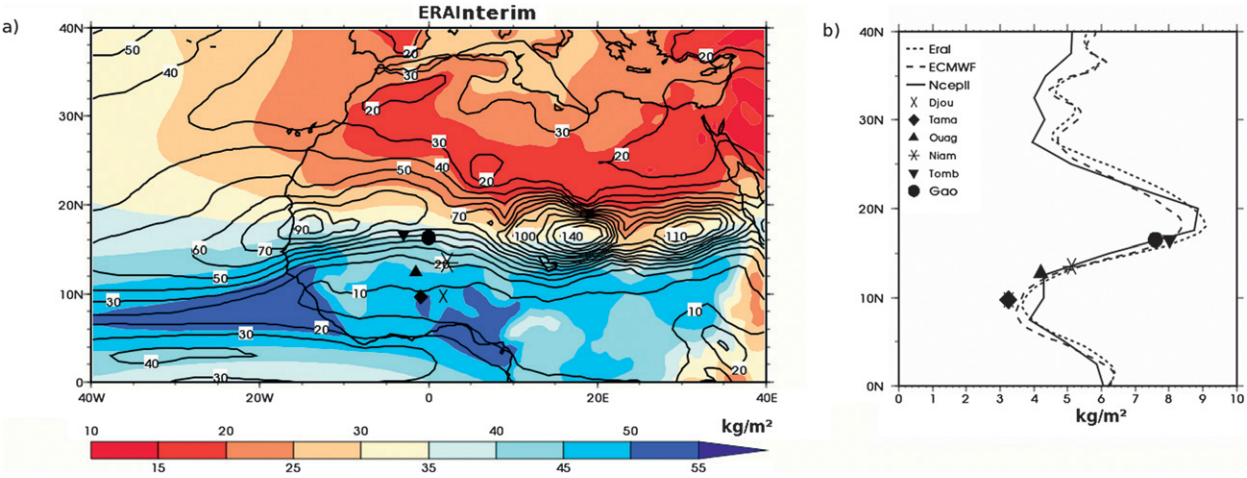

FIG. 1. (a) ERA-Interim JJAS PW mean (kg m^{-2}, shaded) and variance (kg^2 m^{-4}, contours) and (b) 2006 JJAS PW standard deviation (kg m^{-2}) as a function of latitude from different datasets; model data are averaged between 5°W and 5°E. Curves represent ERA-Interim (short dash), ECMWF analysis (long dash), and NCEP (solid). The GPS stations are as follows: Djougou (9.7°N, 1.7°W), Tamale (9.6°N, 0.9°W), Ouagadougou (12.4°N, 1.5°W), Niamey (13.5°N, 2.2°E), Timbuktu (16.7°N, 3°W), and Gao (16.3°N, 0°).

2010 at a 2.5° × 2.5° horizontal resolution. Daily rainfall estimates were provided by the Global Precipitation Climatology Project (GPCP; Huffman et al. 2001).

b. Methods

The diurnal and seasonal cycles are intense over the continent and can perturb the ISV analysis. For any geophysical field α, the diurnal cycle was first removed using a 24-h running average. For the sake of brevity, the notation α was kept, even though the diurnal cycle had been filtered out. Then, the seasonal cycle $\overline{\alpha}^s$ was computed and smoothed[2] using the years 1989–2007 and was subtracted to obtain the intraseasonal anomaly, given as $\alpha^{is} = \alpha - \overline{\alpha}^s$ in the following. No particular treatment was applied to remove interannual variability so that the method could be used in near–real time.

Some of the following analyses involved temporal high-pass, bandpass, and low-pass filtering, based on the Lanczos filter described in Duchon (1979).

Finally, composite anomaly significance was determined using a two-tailed Student's t test at the significance level of 95%.

3. Regional properties of the intraseasonal variability

a. Mean and variance

Figure 1a shows the PW mean climatology and variance for the 1989–2007 summer seasons [June–September (JJAS)]. The largest PW values, above 45 kg m^{-2}, are collocated with the JJAS mean position of the intertropical convergence zone (ITCZ), near 7°–8°N over the Atlantic Ocean. Over the African continent, the largest PW values are located from the Guinea Coast to 12°N, but the PW pattern is more discontinuous, partly because of the topography (see also Fig. 2), as it reaches lower values over the highlands of Ethiopia, Cameroon, and Guinea. PW values are much weaker over the Sahara Desert, where they can fall below 20 kg m^{-2}. In between, a well-defined, strong, north–south gradient arises around the intertropical discontinuity (ITD). The mean PW standard deviation displays large amplitudes, greater than 10 kg m^{-2}, with maxima in the region of this gradient. Three cores of maximum variance strike out along the ITD, at approximately 35°E, 17°E, and 12°W. The discontinuity between the two eastern cores is presumably due to the lower PW value imposed by the presence of the Darfur Mountains. The PW variability zone is not totally steady during the monsoon as the maximum gradient region migrates northward from June to August and then southward in September (Cadet and Houston 1984).

These features of the PW climatology are consistent in NCEP2 and ERA-Interim. Figure 1b shows the meridional distribution of the PW standard deviation, computed for the 2006 summer season using the two reanalyses, the ECMWF operational analyses, and the six GPS station measurements. The three reanalyses capture a latitudinal structure of PW variability that is consistent with the results of Bock and Nuret (2009).

In the following analysis, as in the present section, ERA-Interim and NCEP2 datasets provide consistent

[2] The smoothed annual cycle is obtained through five passes of an 11-day running mean.

results. For the sake of brevity, only ERA-Interim results will be shown and discussed in the following.

b. Intraseasonal variance distribution

The 90-day high-pass filtered variance of PW in Fig. 2a quantifies the variability on intraseasonal time scales. The maximum of variability is still collocated with the gradient of PW in the Sahelian band (12°–22°N) on the northern flank of the African easterly jet (AEJ). Its average pattern is similar to that of the total variance discussed above (Fig. 1a), except that the intraseasonal variance is now equitably distributed in both the eastern and western sides of the Sahel. The zonal asymmetry of the PW total variance is therefore linked to seasonal-to-interannual time scales. On average over the domain 12°–20°N, 10°W–10°E, subseasonal fluctuations account for approximately 55% of the PW total variance, as against 45% over 10°–20°N, 10°–30°E.

Intraseasonal time scales are further decomposed into 10–90-day (Fig. 2b) and 1–10-day ranges (Fig. 2c). The variance for the 10–90-day time scales is maximum between 40° and 10°E, whereas, west of 10°E, it diminishes. In contrast, the synoptic scale (1–10 days) exhibits a variance that grows in the westward direction from 10°E and reaches a maximum at the West African coast, slightly north of Dakar, Senegal. This regional sensitivity was confirmed via a spectral analysis (not shown) with notable peaks having a 5–9-day period in the western part, in agreement with Cadet and Houston (1984). Hence, the Sahel band was sampled in five boxes in order to handle the spatial dependence of the PW variability. The boxes are plotted in Fig. 2c. They cover latitudes from 12° to 20°N, so that the seasonal migration of the gradient zone is always captured. Their 8° latitudinal extension is sufficient to average out geographic heterogeneities.

The time–longitude diagram of Fig. 3a illustrates the evolution of the intraseasonal anomaly PW^{is} in the Sahel band (12°–20°N) for the summer of 2006. PW^{is} is defined following section 2b. The longer periods of intraseasonal variability over the eastern Sahel (east of 10°E) already noted in Fig. 2 are clearly confirmed. The eastern Sahel also appears much dryer until mid-July of 2006 than in the climatology because of the late monsoon onset on 3 July (Janicot et al. 2008). Superimposed on this slow variability, quite regular wet and dry synoptic fluctuations (blue and red stripes, respectively) are clearly visible, traveling westward at about 9 m s^{-1}. Some can be tracked throughout Africa and cross the 80° domain width in about 10 days. Some of these wet events have been documented in details thanks to the African Monsoon Multidisciplinary Analysis (AMMA) observations. For instance, the propagative surge of 6–7 June 2006 (noted ''C'' in Fig. 3) was reported by Couvreux et al. (2010). The coupled convection–AEW event on 25–27 July 2006 (noted ''B'') was studied by Barthe et al. (2010). The wet event preceding the genesis of Hurricane Helene (noted ''H'') over the western Atlantic in late August 2006 can also be tracked during a week over Africa as studied by Schwendike and Jones (2010). Dry fluctuations have been less studied but have similar propagation and correspond to suppressed or localized convection periods (dry spells). The case of the diurnal cycle of convection observed over Niamey on 10 July and extensively documented by Lothon et al. (2011) illustrates this type of convection organization occurring during dry periods (noted ''L'').

Such wet and dry synoptic events occurring on the northern flank of the AEJ often seem to be closely connected with AEWs. This is confirmed by the computation of correlations between PW^{is} and the meridional wind or the relative vorticity anomalies at different levels used to detect AEWs. The correlation is stronger with the meridional wind than with the vorticity. It is maximum for the 850-hPa level. The latter correlation is weaker (0.55) over the eastern Sahel; it then increases westward to reach a maximum of 0.75 at the coast when the meridional wind leads PW by about half a day. To illustrate this relationship between AEWs and wet and dry synoptic events, Fig. 3b provides the same time–longitude diagram as Fig. 3a for the 850-hPa meridional wind. Like PW anomalies, anomalies are growing and moving westward at about 9 m s^{-1}. The three cases noted previously (C, B, and H) are also characterized by strong positive meridional wind anomalies.

As further discussed in the next sections, PW synoptic anomalies are presumably the moisture footprint of AEWs. Their properties are quite similar to those of AEWs, when a more traditional kinematic predictor is used (meridional wind or vorticity). Nevertheless, PW provides a complementary and integrated approach to AEWs, which essentially selects those that maximize the moisture content of the column (i.e., those for which the dynamics and diabatic effects have a certain degree of consistency in the vertical direction).

4. PW footprint of African easterly waves

a. Composite building

In this section, the analysis is based on indices computed from the 10-day high-pass filtered PW anomalies averaged over each box shown in Fig. 2c. We recall that the diurnal cycle is removed in the following analysis (see section 2b). This filtering window was chosen to give insight into the fluctuations of PW induced by AEW

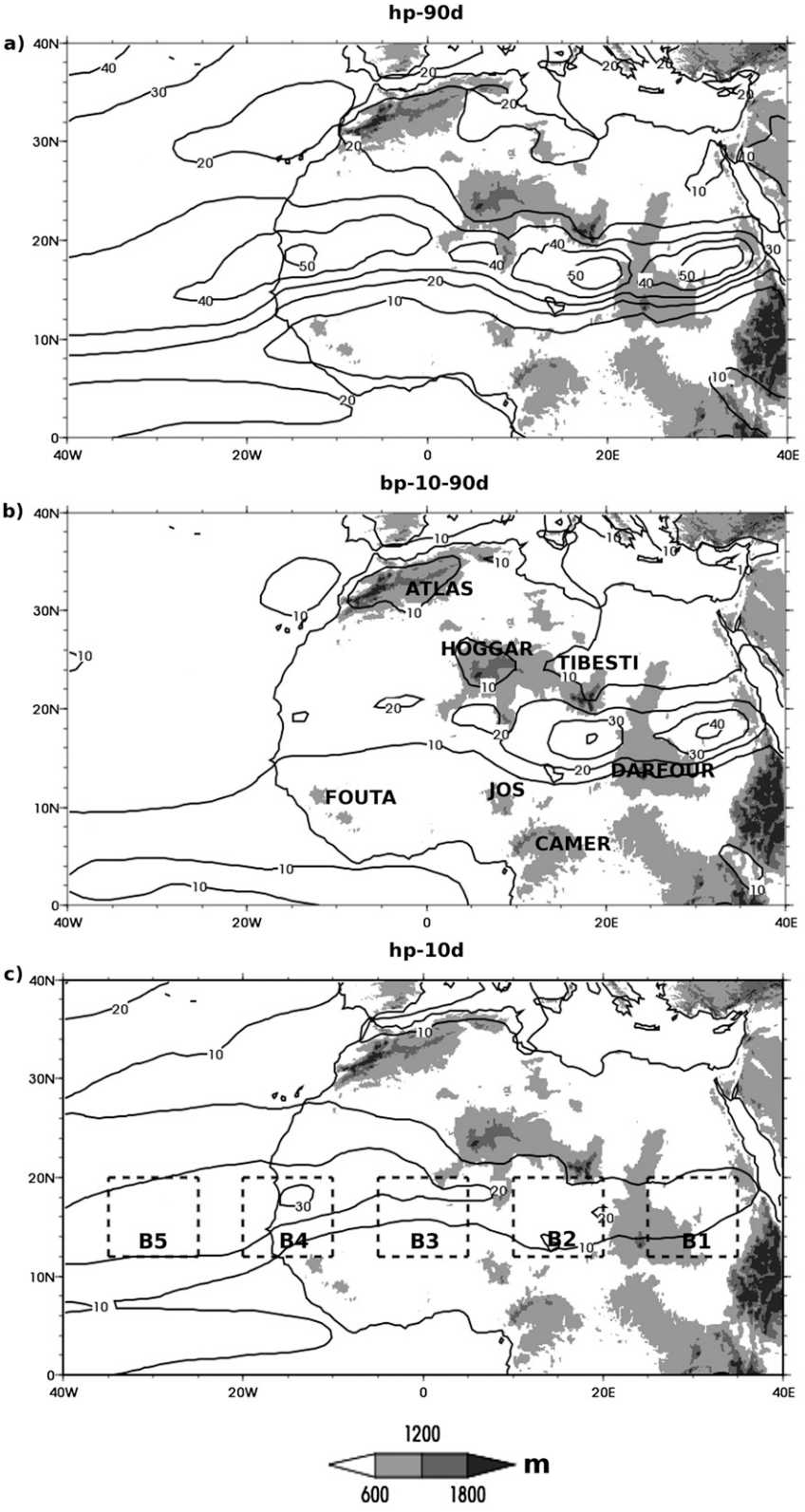

FIG. 2. (a) PW 90-day high-pass filtered variance ($kg^2\ m^{-2}$, contours) averaged over the JJAS summers from 1989 to 2007. (b) As in (a), but for 10–90-day variance. (c) As in (a), but for 10-day high-pass filtered variance. The five boxes described in section 3 are displayed in (c). Topography (m) is shaded.

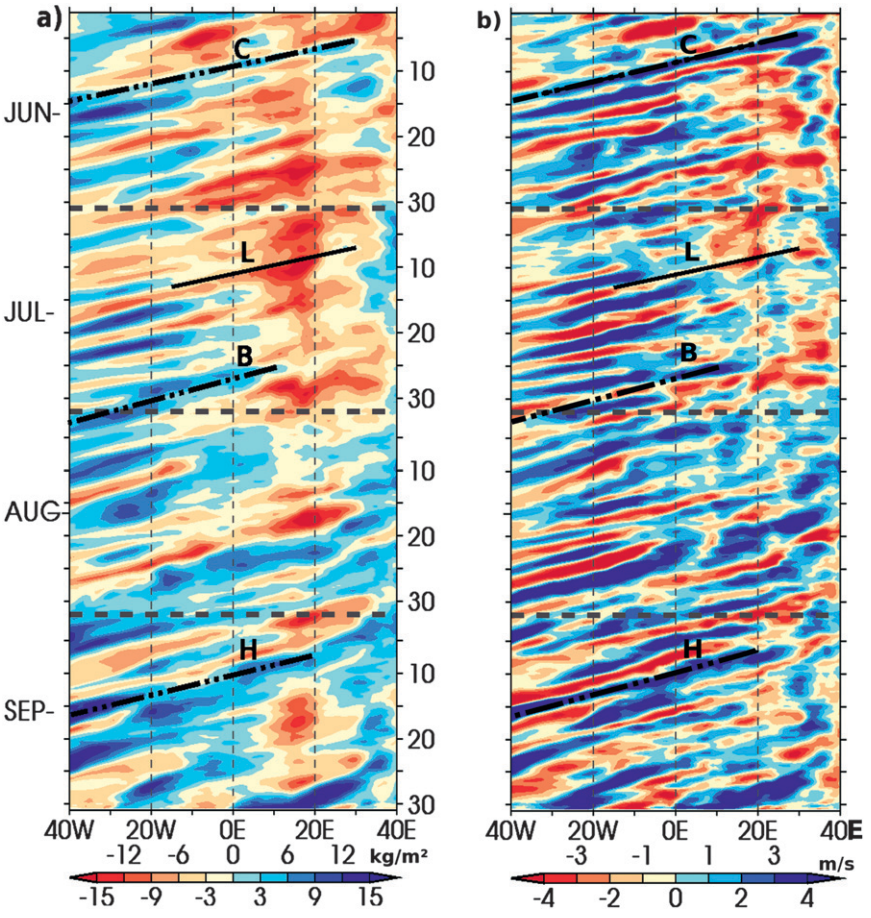

FIG. 3. Time–longitude diagram of the 2006 JJAS intraseasonal anomalies averaged over 12°–20°N: (a) PW (kg m^{-2}) and (b) 850-hPa meridional wind (m s^{-1}). The black solid lines materialize a slope of a 9 m s^{-1} velocity. C, L, B, and H refer to events referenced in section 3.

activity. The main time scale of PW fluctuations is estimated using the lag autocorrelation of the index of a given box (Fig. 4a). In each region, the period is close to 5–6 days, as already suggested in the analysis of Fig. 3a. The lag correlation between two contiguous domains (with a 1.5–2-day lag) emphasizes a westward propagation of PW anomalies (Fig. 4b) of about 9 m s^{-1}, consistent with the AEW literature (e.g., Kiladis et al. 2006). Over the eastern Atlantic, the propagative component is strongest, as indicated by the highest correlation between boxes 4 and 5. These properties are consistent with those suggested by Fig. 3a for the summer of 2006, particularly after the late monsoon onset on 3 July (Janicot et al. 2008).

For each Sahel box, the corresponding PW^{is} index defines particularly wet (dry) events when it exceeds plus (minus) one standard deviation and is maximum (minimum). Note that the standard deviation is computed over all summers from 1989 to 2007, and is box dependent. Wet and dry events have rather symmetric characteristics. Those associated with western boxes are more intense and more frequent than those associated with eastern boxes. On average, 4–5 wet events and 4–5 dry events are recorded each month. According to several sensitivity tests (not shown), these properties are robust, with little dependence on the period of the season, the chosen latitude band, or the filtering window.

For these sets of wet (subscript w) and dry (subscript d) events, Ω_w and Ω_d, the composite operator (noted by a superscript asterisk) applied to any variable α at a time lag δt is defined as

$$\alpha_w^*(t_0+\delta t)=\frac{1}{N_w}\sum_{t\in\Omega_w}\alpha^{\mathrm{is}}(t+\delta t)\quad\text{and}$$

$$\alpha_d^*(t_0+\delta t)=\frac{1}{N_d}\sum_{t\in\Omega_d}\alpha^{\mathrm{is}}(t+\delta t),$$

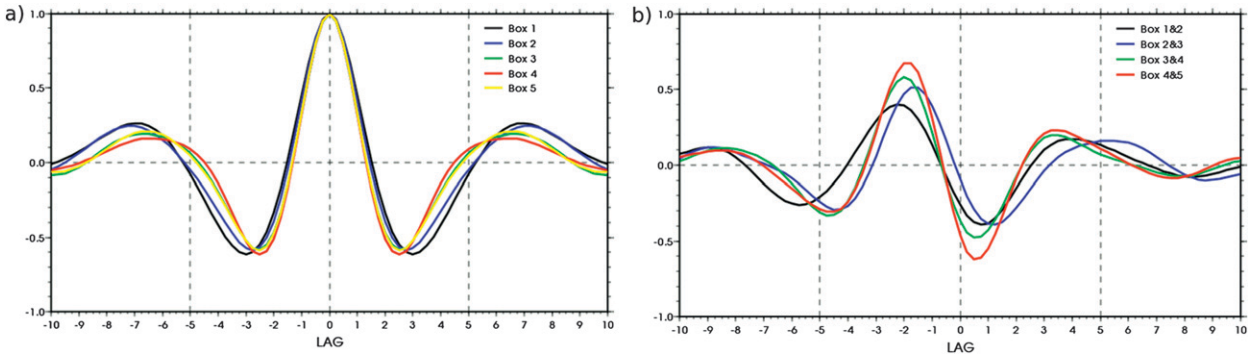

FIG. 4. (a) Autocorrelations of the 10-day high-pass filtered PW indices. (b) Lag correlation between two indices corresponding to two neighboring boxes; the eastern one leads. The five boxes are displayed in Fig. 2c.

where t_0 is the time reference of the composite and N_w and N_d are the number of wet and dry events, respectively. Note that the composite operator is applied to intraseasonal anomalies. The 10-day high-pass filtering was only used to define the events. As wet and dry composites are almost symmetric, only their mean magnitude $\alpha^* = (\alpha_w^* - \alpha_d^*)/2$, significant at the 95% level, will be shown. We will focus on box B3, which corresponds to the AEW growing zone (e.g., Hall et al. 2006), with the strongest low-level temperature and humidity gradients, and where GPS observations were available.

b. *Composite structure*

1) HORIZONTAL STRUCTURE

Figure 5 shows the composite structure at t_0 of PW and the 925-hPa horizontal wind ($\mathbf{U}_{925}$, $\mathbf{V}_{925}$) anomalies, noted PW* and ($\mathbf{U}^*_{925}$, $\mathbf{V}^*_{925}$), respectively (section 4a). The wet anomaly covers a domain larger than B3, extending from 10° to 25°N. It corresponds to a 15% modulation (~5 kg m^{-2}) of the JJAS mean PW. Two dry anomalies flank this positive anomaly to the east and west, the western one being more intense. South of 10°N, anomalies of opposite sign occur and the northern Sahel humidification partly corresponds to a northward displacement of the mean PW maximum latitudinal band. The horizontal low-level wind composite anomaly is consistent with the PW* patterns as northward wind anomalies, indicating a strengthening of the moist monsoon flow, are maximum on the western side of the wet anomalies. Figure 6 describes the time evolution of PW* and V^*_{925} anomalies. The PW* maximum in B3 at t_0 is detectable 5 days before, near 30°E with a weak but significant intensity. West of this maximum, a minimum of humidity occurs consistently with dry northerly surges.

At $t_0 - 3$, these two structures are displaced westward with an intense southerly low-level wind anomaly helping to feed the moist anomaly. Between $t_0 - 1$ and $t_0 + 1$, B3 is crossed by the positive anomaly tilted in the northeast–southwest direction while the negative one reaches the Atlantic Ocean. Progressively, the wet anomaly moves toward the ocean at $t_0 + 5$.

Figure 7 summarizes the spatiotemporal evolution of both PW* and V^*_{925} in a Hovmöller diagram. The humidity anomaly can be tracked 4 days before it reaches the Greenwich meridian and more than 5 days after, from about 25°E to the eastern and central Atlantic. It is preceded and followed by dry but weaker anomalies. The wind structure is 1–2 days ahead, suggesting that low-level advection is an important process for moistening the atmospheric column. The robustness, consistency, and spatial footprint of PW anomalies imply potential short- to medium-range predictability of the associated wet and dry events.

To further validate our results, especially with regards to the accuracy of the ERA-Interim, composites of the

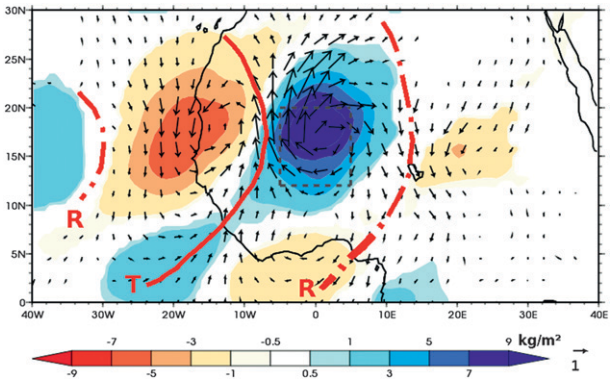

FIG. 5. Composite structure based on the B3 index at t_0: PW (kg m^{-2}) is shaded and arrows represent the 925-hPa wind anomalies (m s^{-1}). Note that only the 95%-significant half-difference between positive and negative events is plotted. The red lines indicate the 600-hPa trough (T, solid line) and ridge (R, dashed–dotted line).

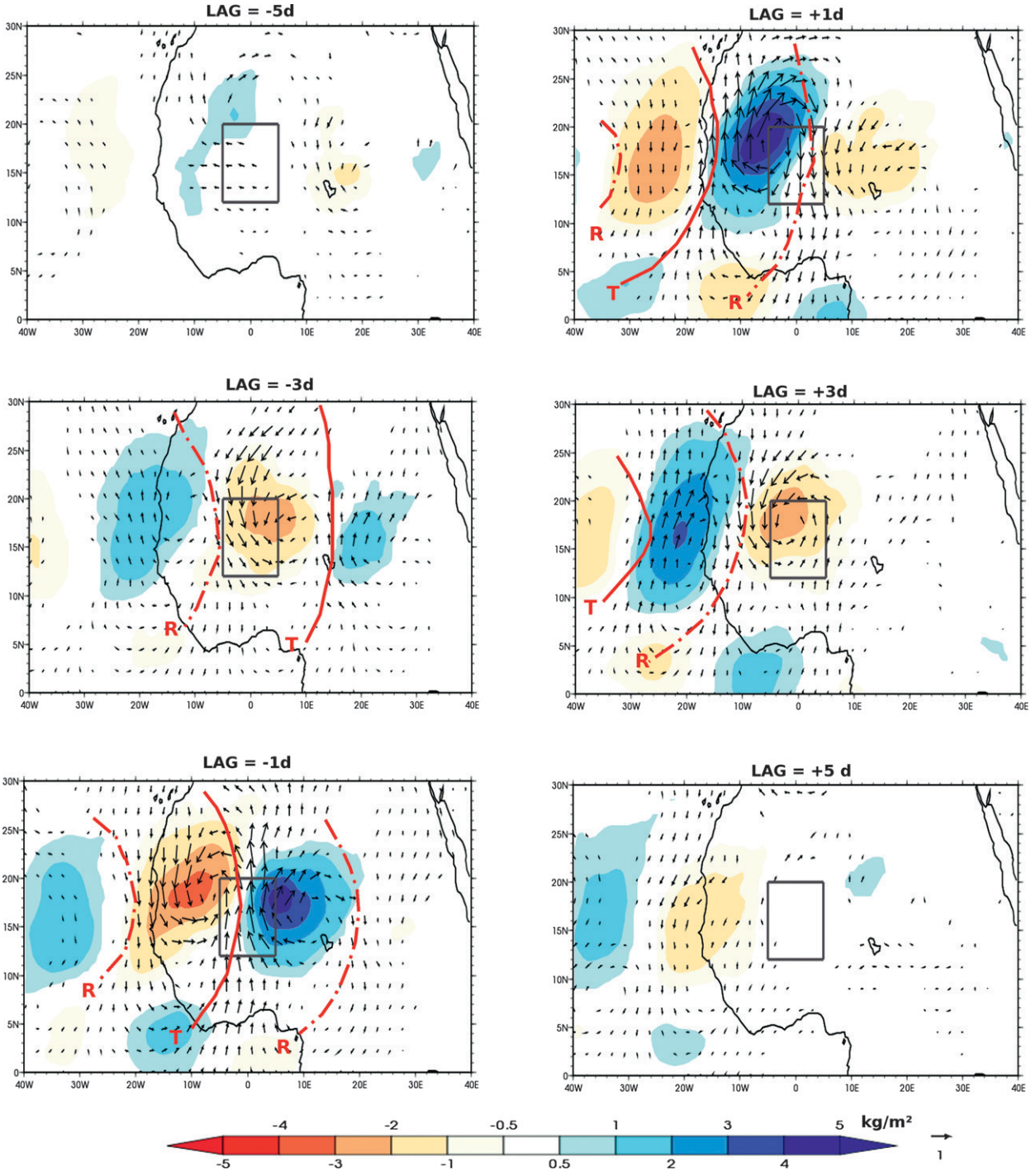

FIG. 6. As in Fig. 5, but for lags from $t_0 - 5$ to $t_0 + 5$, with a 2-day time step.

PW derived from the ground-based independent GPS data are presented in Fig. 8, for the summer of 2006, at the four stations shown in Fig. 1. Note that no radiosonde measurements are taken at Gao (16°N, 0°), so the ERA-Interim PW is even more independent of the GPS retrieval. Except for two cases during 2006, the detection of events with the reanalysis at the B3 scale is in agreement with local in situ observations. The wet and dry event detection is more accurate at the beginning and the end of the season when PW fluctuations

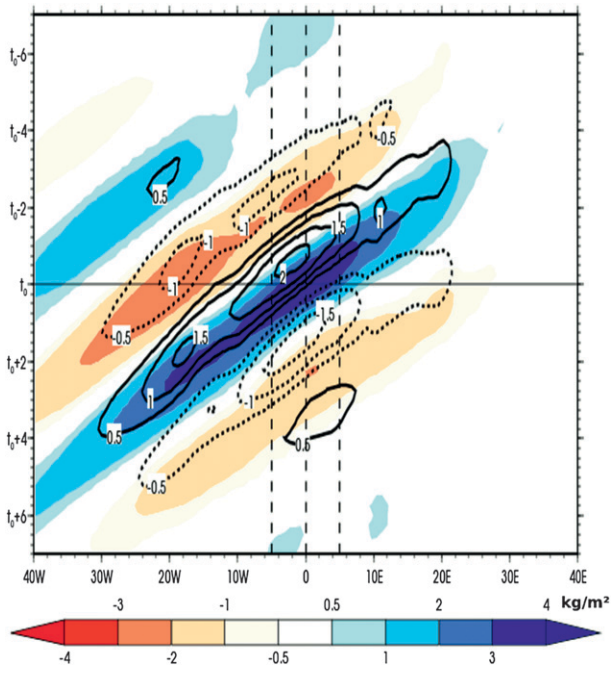

FIG. 7. Lag–longitude composite structure averaged over 12°–20°N of PW (kg m^{-2}, shaded) and 925 hPa V (m s^{-1}, contours) anomalies. The vertical dashed lines correspond to the delimitation of B3.

are larger. The composites of GPS data and ERA-Interim in Figs. 8b and 8c are similar both in intensity and in phase relationship at the different locations. The southern stations (Niamey and Ouagadougou) show weaker PW* anomalies than do the northern ones (Gao and Timbuktu), which is in agreement with a maximum PW anomaly around 18°N. Also the time shift of the anomaly maximum between Niamey (2.2°E) and Timbuktu (3°W) observed by GPS confirms the westward propagation.

The AEW properties from this PW perspective are rather similar to those derived on the northern flank of the AEJ in earlier studies (e.g., Reed et al. 1977; Kiladis et al. 2006). For instance, Kiladis et al. (2006) found a wavelength in the range of 3600 km, close to the one that can be computed here (~3800 km) and a period of 4.8 days, slightly shorter than the 5–6 days found here. The slower phase speed over the Atlantic is noticeable on the 925-hPa wind composite anomalies but not on PW anomalies, which are more in phase with the low-level wind (Fig. 7).

2) VERTICAL STRUCTURE

The present section investigates the vertical structure of the wet and dry events, with fields averaged over a narrower longitude extent (2°W–2°E) in order to reduce smoothing of the wave structure. The evolution of the specific humidity vertical structure in Fig. 9a indicates that the PW composite results from a moist anomaly at all levels of the atmosphere. The maximum of humidification is stacked up between the surface and 700 hPa consistently with Fig. 3a of Couvreux et al. (2010), although the midlevel (700–400 hPa) relative contribution to the PW composite anomaly is larger than the contribution to the PW seasonal mean (not shown). The wet event is preceded and followed by contrasting dry events by 2.5 days. The meridional wind anomaly is vertically tilted, leading PW* by 1 day close to the surface and in phase at the AEJ level (600 hPa). This rearward tilt of the trough is typical of baroclinic conversion (Thorncroft and Hoskins 1994). At 700 hPa, the trough leads the humidity maximum by 1.25 days, confirming previous studies (e.g., Kiladis et al. 2006) in which rainfall was shown to occur behind the trough in the northward moistened flow.

The potential temperature and vertical velocity anomalies (Fig. 9b) are negative and large below the AEJ level (600 hPa). At the passage of a wet event, the atmosphere is moister (+1 g kg^{-1}) and colder (−1 K) while the mean vertical ascent (see Fig. 12c) becomes a relatively strong subsidence below 600 hPa (anomaly of −5 mm s^{-1} for a mean state value of about 2–3 mm s^{-1}). Above, opposite but much weaker structures are observed, which, consistently with a moist, warm anomaly, may indicate a reinforcement of deep convection. The configuration is reversed 2.5 days before and after the wet event, so warming occurs below 600 hPa, whereas, above, a slight negative anomaly of vertical motion reduces the deep convection. According to the hydrostatic hypothesis, this structure of the temperature anomaly below 600 hPa implies the evolution of the surface pressure (Fig. 9d) with a reinforcement of the heat low (−1 hPa) in the Sahel band 2 days before the wet event, its rapid collapse (+1 hPa) during the event, and its recovery (−0.5 hPa) after, as shown in Couvreux et al. (2010). As suggested by Fig. 9e, the composite low-level meridional wind is almost geostrophic (when the diurnal cycle has been removed). Its maximum southerly (northerly) anomaly occurs 1 day before (after) the wet event and is mainly in equilibrium with the fluctuations of the surface pressure zonal gradient.

Figure 9c shows the lag–height profiles of relative humidity with relatively large anomalies (±15%) occurring above 500 hPa. This corresponds to an expected strong signature of such events in terms of upper-level cloudiness, and thus OLR, and a large impact on the radiative budget sensitive to relative humidity (Roca et al. 2011). The zonal wind anomalies (Fig. 9c) are weaker than the meridional ones. Nevertheless they result in a rearward-sloping sharp convergence zone partly consistent with the positive vertical velocity

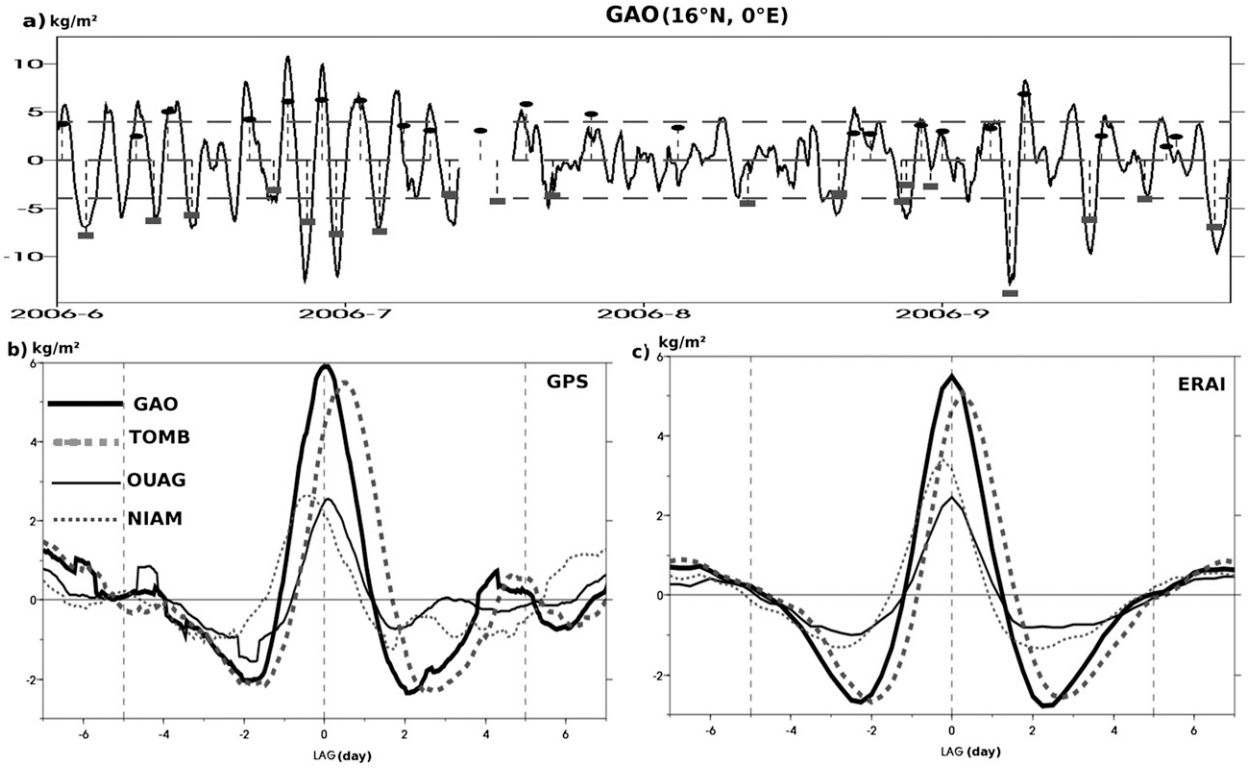

FIG. 8. GPS observations: (a) 2006 Gao GPS time series of PW 10-day high-pass filtered intraseasonal anomalies (black curve). Vertical dash lines indicate dates and intensities of dry and wet events identified with ERA-Interim. (b) PW composites computed from GPS measurements at Gao (16°N, 0°), Timbuktu (16.7°N, 3°W), Ouagadougou (12.4°N, 1.5°W), and Niamey (13.5°N, 2.2°E). (c) As in (b), but with the ERA-Interim.

anomaly (Fig. 9b). The midlevel westward acceleration combined with subsidence under 600 hPa between t_0 and $t_0 + 1$ may be the footprint at large scale of the rear inflow observed behind convective systems with trailing stratiform precipitation (Smull and Houze 1987; Lafore and Moncrieff 1989; Diongue et al. 2002; Barthe et al. 2010). Above, the meridional wind anomaly at 600 hPa is weakly geostrophic (Fig. 9f).

A salient feature of this composite vertical structure is the fact that wet (dry) events are preceded by a dry (wet) event, as already highlighted in Fig. 5. This helps to accelerate the low-level meridional wind northward (southward) ahead of the event and thus contributes to its propagation and intensification.

3) CONVECTIVE ACTIVITY MODULATION

To assess the relation between the synoptic wet and dry events and convection, GPCP rainfall and OLR composites are displayed in Fig. 10 from $t_0 - 3$ to $t_0 + 2$. At t_0 rainfall increases in B3 with a maximum anomaly of 2.5 mm day^{-1} slightly leading the wet PW anomaly. To both the west and east, negative precipitation anomalies match the dry areas. OLR anomalies also indicate large modulation of convective activity in the region of maximum PW gradient. OLR anomalies extend farther north than GPCP precipitation anomalies, up to 25°N, which might be a signature of nonprecipitating convective systems and of the wet anomaly itself. As for PW anomalies, convection intensification can be tracked 3 days earlier from the Sudan region, and 3 days later when it reaches the Senegalese coast and the Atlantic. As in Fig. 5, the precipitation composite exhibits antisymmetric anomalies south of 10°N, such that a precipitation enhancement in the Sahel is associated with a precipitation weakening to the south, corresponding to a northward shift of the ITCZ. The OLR structure resembles the AEW analysis north of the AEJ as shown in Kiladis et al. (2006, their Fig. 4). In particular, the troughs and ridges at 600 hPa (labeled ''T'' and ''R,'' respectively, on Fig. 10) indicate that precipitation positive anomalies occur behind the trough over the Sahel but around it toward the coast and over the Sudanese band (south of 10°N).

Figure 10d assesses the capability of ERA-Interim precipitation to capture the strong (±30%) convective modulation observed (for a seasonal mean of 3 mm day^{-1}).

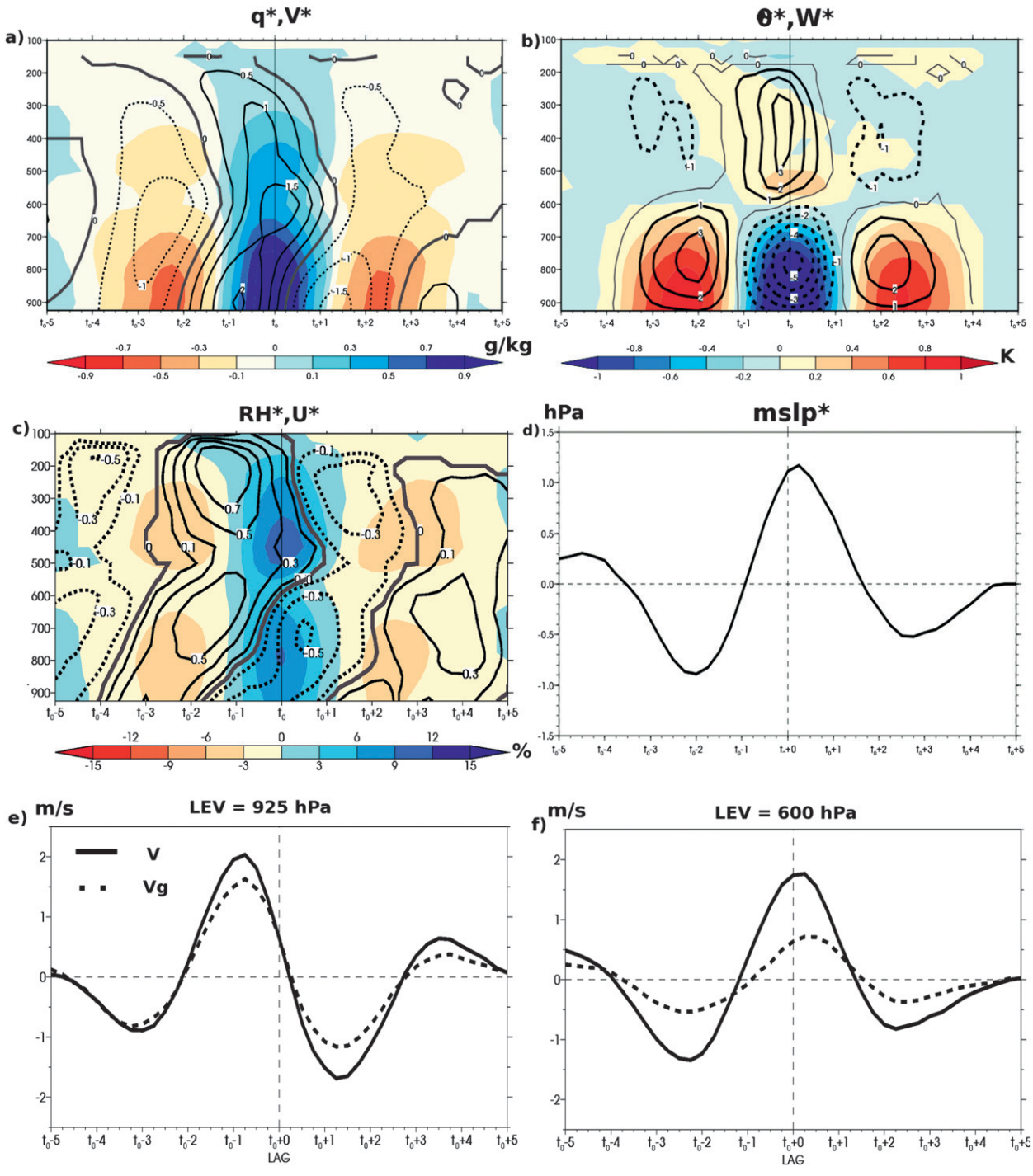

FIG. 9. Vertical–lag composite of (a) specific humidity (g kg^{-1}, shaded) and meridional wind (m s^{-1}, contours) anomalies, (b) potential temperature (K, shaded) and vertical wind (mm s^{-1}, contours) anomalies, and (c) relative humidity (%) and zonal wind (m s^{-1}, contours) anomalies. Lag evolution of (d) mean sea level pressure (hPa) and (e) 925-hPa meridional wind (m s^{-1}, solid line) and geostrophic meridional wind (dotted line) anomalies. (f) As in (e), but at 600 hPa. All fields are spatially averaged over 12°–20°N, 2°W–2°E.

Overall, the qualitative agreement is remarkable, even though ERA-Interim is unable to accurately reproduce the rainfall temporal phase shift together with the PW maximum (rainfall is 6–12 h ahead) and the satellite-derived precipitation intensity. This consistency of ERA-Interim precipitation with observations allows us to use the reanalysis for further analysis of the AEW moisture budget.

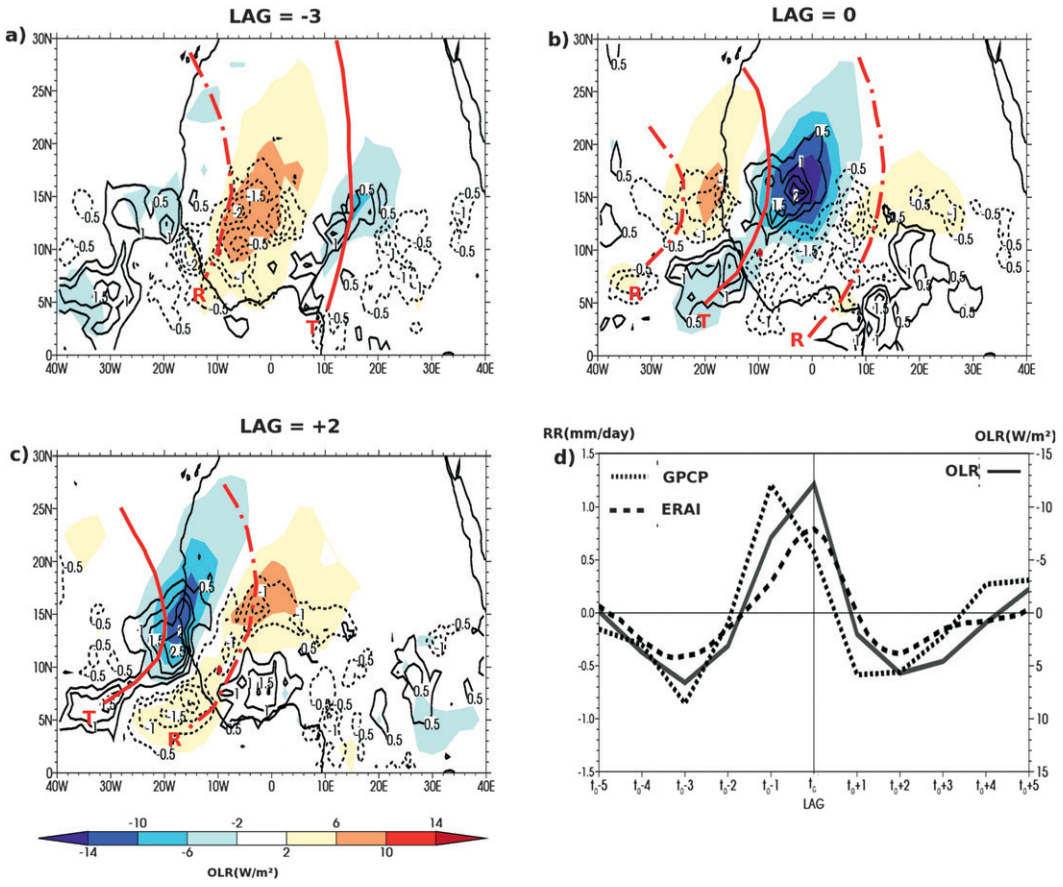

FIG. 10. Composites of NOAA OLR (W m^{-2}, shaded) and GPCP rainfall (mm day^{-1}, black contours) anomalies at (a) $t_0 - 3$, (b) t_0, and (c) $t_0 + 2$. The red lines indicate the AEW 600-hPa trough (T, solid line) and ridge (R; dashed–dotted line). (d) Lag evolution of NOAA OLR (W m^{-2}, solid line), GPCP rainfall (mm day^{-1}, dotted line), and ERA-Interim rainfall (mm day^{-1}, dashed line) anomalies in the 12°–20°N, 2°W–2°E box.

5. Moisture budget analysis of AEWs in ERA-Interim

In this section, our main goal is to compute a composite budget of integrated moisture during the life cycle of wet and dry events induced by AEWs, so as to give insight into the key processes involved during the different AEW phases.

a. Budget equations

The equation of the moisture evolution can be written in generic form as

$$\frac{\partial q}{\partial t} = -u_i \frac{\partial q}{\partial x_i} + D_{\text{iab}} q + \varepsilon_q, \qquad (1)$$

where the first term on the right-hand side represents the total advection (Einstein notation), and the second, $D_{\text{iab}}q$, stands for all diabatic terms such as water phase changes (condensation, evaporation, sublimation, . . .), subgrid turbulence, and convective eddies. The total moisture tendency and the advection terms are computed from ERA-Interim at each grid point every 6 h. The residual term contains the total diabatic term computed by the model itself, and also an unknown "closure" term ε_q due, for instance, to the increments of each assimilation process, or to the discretization. In consequence, only the total $D_{\text{iab}}q + \varepsilon_q$ is estimated and used in the following analysis.

The seasonal cycle and seasonal anomaly operators defined in section 2 are then applied to (1), so that the moisture budget composite can be computed

$$\frac{\partial q^*}{\partial t} = \left(-u\frac{\partial q}{\partial x}\right)^* + \left(-v\frac{\partial q}{\partial y}\right)^* + \left(-w\frac{\partial q}{\partial z}\right)^* + D_{\text{iab}}q^* + \varepsilon q^*. \qquad (2)$$

The PW* budget is finally derived from the vertical integration of (2):

$$\frac{\partial \text{PW}^*}{\partial t} = A_x^* + A_y^* + A_z^* + E^* - P^* + \text{CLSR}^*, \qquad (3)$$

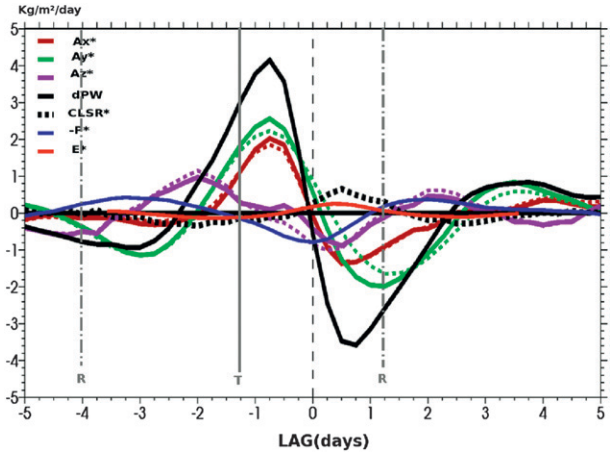

FIG. 11. Integrated humidity composite budget (kg m^{-2} day^{-1}) in the 12°–20°N, 2°W–2°E box. Legend shows the contributions of each term of the budget (see the text). Solid lines are the total contribution of each advective term and the dashed lines are their linear contribution. The vertical gray lines indicate the AEW 600-hPa trough (T, solid) and ridge (R; dashed–dotted).

where A stands for advection terms, and E and P are the surface evaporation and precipitation rates, respectively. The last term, CLSR, represents the budget closure that will be checked.

To analyze the advection terms it is useful to compute the contribution of "linear" terms by taking the JJAS seasonal mean as a basic state. According to this hypothesis, the linear advection terms can be written as two vertical integrations over the domain depth H:

$$\mathrm{LIN}.A_i^* = -\int_0^H \left(\overline{u}_i^s \frac{\partial q^{\mathrm{is}}}{\partial x_i}\right)^* \rho\, dz - \int_0^H \left(u_i^{\mathrm{is}} \frac{\partial \overline{q}^s}{\partial x_i}\right)^* \rho\, dz. \quad (4)$$

b. Analysis of the PW budget

The PW* budget is computed using (3), along the Greenwich meridian, and the composite evolution of each term is shown in Fig. 11. The maximum moist anomaly reached at t_0 results from an intense moistening, which culminates at +4 kg m^{-2} day^{-1} 12 h after the midlevel trough (i.e., 18 h before t_0). It is followed by an intense, almost symmetric, drying after the event maximum, 12 h before the ridge. The budget closure is always weaker (below 0.5 kg m^{-2} day^{-1}) than the dominant terms (advection terms).

The column moistening is mainly due to advection terms (Fig. 11). It is initiated first by the vertical advection anomaly A_z^*, which peaks at +1 kg m^{-2} day^{-1} 2 days before t_0, as the heat low extends to the south. Then, between $t_0 - 2$ and $t_0 - 1$, as the AEW midlevel trough passes over the Greenwich meridian, the underlying enhanced cold and moist monsoon flow pushes the heat low northward, contributing more than half of the column moistening A_y^* (+2.8 kg m^{-2} day^{-1}). The zonal advection A_x^* (2 kg m^{-2} day^{-1}) closely follows the meridional term. Rainfall ($-P^*$) starts 1 day before t_0, just after the trough passage, in the northerly flow, and helps to damp the PW anomaly. As ERA-Interim precipitation is slightly late in the composite, this effect might be expected to occur 1 day earlier. The vertical advection reverses and further induces the disappearance of the PW wet anomaly as the AEW ridge approaches. Overall, surface evaporation seems to play a minor role.

Advection terms are mainly explained by their linear part as computed from (4) (dotted lines in Fig. 11), except for the meridional advection during the drying of the moist event and the vertical advection around t_0.

To summarize, at first order, the occurrence of the PW wet anomaly is well explained linearly by the AEW dynamics, with a small precipitation contribution. We will now investigate the extent to which these linear and adiabatic properties remain valid at each altitude, as the PW anomaly was shown to correspond to moisture anomalies that were strongly consistent with the height.

6. Linear adiabatic analysis of PW anomalies

In the present section, a linear adiabatic analysis of the PW equation is used to highlight the major mechanisms involved in the growth and propagation of PW anomalies.

a. Equations

Linear and adiabatic terms have been shown to explain quantitatively the first-order integrated moisture budget evolution. This property is exploited to evaluate how a simple linear and adiabatic diagnostic approach based on the AEW dynamics could capture the evolution of humidity at each vertical level. From (4), the linearized adiabatic version of the q^* tendency in (3) becomes

$$\frac{\partial q^*}{\partial t} = -\left(\overline{u}_i^s \frac{\partial q^{\mathrm{is}}}{\partial x_i}\right)^* - \left(u_i^{\mathrm{is}} \frac{\partial \overline{q}^s}{\partial x_i}\right)^*. \quad (5)$$

To obtain an analytic solution, it is convenient to replace the mean seasonal reference state $\overline{u}_i^s$, which evolves slowly through the season, by a constant reference state taken as the climatological mean $\overline{u}_i$ over the season considered, so that (5) becomes

$$\frac{\partial q^*}{\partial t} = -\overline{u}_i \frac{\partial q^*}{\partial x_i} - u_i^* \frac{\partial \overline{q}}{\partial x_i}. \quad (6)$$

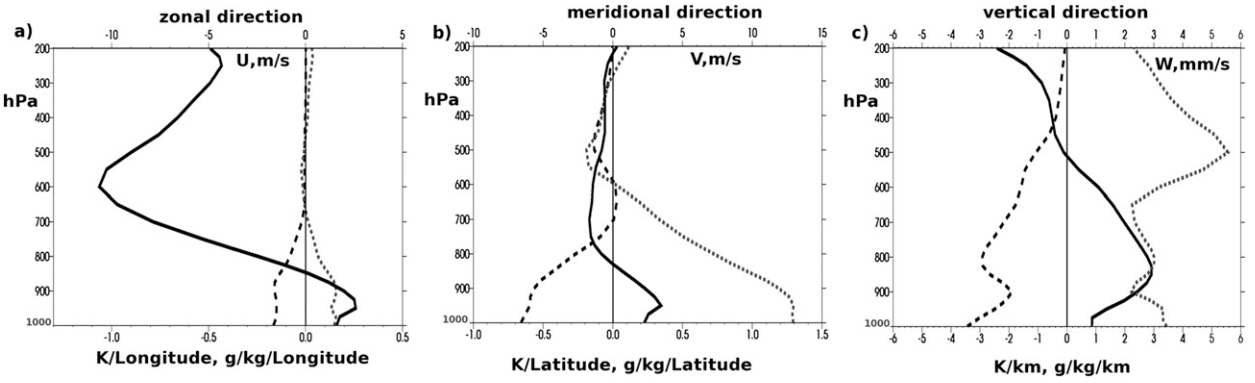

FIG. 12. JJAS mean vertical profiles averaged in the 12°–20°N, 2°W–2°E box of winds (solid lines), potential temperature gradients (dotted lines), and specific humidity gradients (dashed lines)—(a) in the zonal direction: U (m s^{-1}), $\partial\theta/\partial x$ (K per 1° longitude), and $\partial q/\partial x$ (g kg^{-1} per 1° longitude); (b) in the meridional direction: V (m s^{-1}), $\partial\theta/\partial y$ (K per 1° latitude), and $\partial q/\partial y$ (g kg^{-1} per 1° latitude); and (c) in the vertical direction: w (mm s^{-1}), $\partial\theta/\partial z$ (K km^{-1}), and $\partial q/\partial z$ (g kg^{-1} km^{-1}).

A computation of all right-hand-side terms (justification is given in the next subsection) shows that only three terms are important, leading to

$$\frac{\partial q^*}{\partial t} = -\overline{u}\frac{\partial q^*}{\partial x} - v^*\frac{\partial \overline{q}}{\partial y} - w^*\frac{\partial \overline{q}}{\partial z}. \quad (7)$$

This final moisture equation has plane wave solutions in the zonal direction of the form $q^* = \hat{q}^* e^{i(kx-\omega t)}$ (with complex notation), where $\hat{q}^*$ is the modulus of q^*, k is the zonal wavenumber, and ω is the pulsation. We assume that composite variables v^* and w^* can be written in the same way—that is, $v^* = \hat{v}^* e^{i(kx-\omega t+\varphi_v)}$ and $w^* = \hat{w}^* e^{i(kx-\omega t+\varphi_w)}$, where ϕ_v and ϕ_w are the phase shifts relative to the humidity wave at a given vertical level. Solving (7) provides the phase velocity U_φ and the growth rate G_r of the wave:

$$U_\varphi = \overline{u} - \frac{1}{k\hat{q}^*}(\hat{A}_y \sin\varphi_v + \hat{A}_z \sin\varphi_w) \quad \text{and} \quad (8)$$

$$G_r = \frac{1}{\hat{q}^*}(\hat{A}_y \cos\varphi_v + \hat{A}_z \cos\varphi_w), \quad (9)$$

where $\hat{A}_y = |-\hat{v}^*(\partial\overline{q}/\partial y)|$ and $\hat{A}_z = |-\hat{w}^*(\partial\overline{q}/\partial z)|$ are the moduli of the meridional and vertical advections, respectively. Only anomalies contribute to the second term of the phase velocity so it will be referred to as the intrinsic velocity.

The ''observed'' growth rate of humidity anomalies is diagnosed at each level from the specific humidity composite as the rate of amplification of a given maximum (or minimum) during its westward propagation. Similarly, an observed growth rate, constant with height, can be computed based on PW anomalies only.

b. Results and discussion

Figure 12 provides the vertical profiles of various quantities associated with the climatological (JJAS) reference state of the above simple linear analysis on the Greenwich meridian. The zonal wind profile $\overline{u}$ (Fig. 12a) exhibits the well-known features that occur during the monsoon, with the westerly monsoon flux at low level (up to 2.5 m s^{-1}) and the AEJ at 600 hPa (up to 10 m s^{-1}). In agreement with the strong zonal symmetry of the African monsoon, the zonal gradients of temperature and specific humidity are weak (less than 0.2 K and 0.2 g kg^{-1} per 1° longitude), implying that only the advection of the moisture zonal gradient anomaly by the mean zonal wind $[-\overline{u}(\partial q^*/\partial x)]$ will contribute to (7). In the meridional direction, we have the opposite situation with the southerly monsoon flux (3 m s^{-1}) at low level surmounted by a weak reverse flow (-1 m s^{-1}), whereas the temperature and humidity meridional gradients are intense and opposite (up to 1.3 K and –6 g kg^{-1} per 1° latitude at the surface). This strong meridional baroclinicity up to 600 hPa is consistent with the AEJ maintenance (Thorncroft and Blackburn 1999). In consequence, the advection of the mean meridional moisture gradient by meridional wind anomalies $[-v^*(\partial\overline{q}/\partial y)]$ will be the second major linear contribution [in (7)]. The mean vertical velocity of the reference state is ascending (3 mm s^{-1}) below 500 hPa and weakly subsiding above. The vertical stratification is strong, corresponding to a stable atmosphere (3–5 K km^{-1}) and a vertical decrease of the specific humidity maximum at low level (-3 g kg^{-1} km^{-1}). Also, as the vertical motions w^* associated with the mode are intense (up to 6 mm s^{-1}) and the vertical gradient of moisture anomaly is weak, the last major linear contribution in (8) comes from $-w^*(\partial\overline{q}/\partial z)$. At this point, it is worth noting

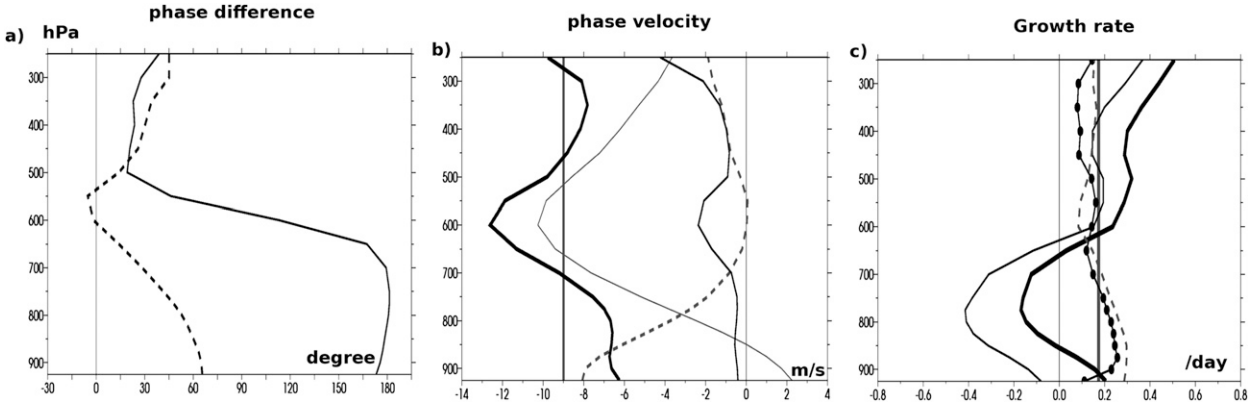

FIG. 13. Linear adiabatic analysis results. (a) Vertical profiles of phases (°) with respect to specific humidity of meridional wind (dashed) and vertical wind (solid). (b) Vertical profiles of propagation velocity (m s^{-1}): meridional (dashed), vertical (black thin solid), and zonal (gray thin solid) contributions and total propagation velocity (black thick solid); the vertical gray thick line indicates the observed propagation velocity of -9 m s^{-1}. (c) Vertical profiles of the growth rate (day^{-1}): meridional (dashed) and vertical (black thin solid) contributions and total growth rate (black thick solid); the observed growth rate computed from the specific humidity at each level corresponds to the dotted black line and the vertically constant growth rate computed from PW corresponds to the gray thick solid line at 0.19 day^{-1}.

that temperature and humidity gradients have opposite signs in each of the three directions. Consequently, these mass and humidity fields will be anticorrelated at least for dynamic processes, so the present analysis performed on the humidity field and the resulting conclusions can be extrapolated to the mass field by replacing moist and dry by cold and warm, respectively.

Looking at the physical interpretation of G_r and U_φ of our linear analysis [(8) and (9)], the determination of phase shifts between the q^* event and $v^*(\phi_v)$ and w^* (ϕ_w) are critical. If v^* is in phase with q^* ($\phi_v = 0$) it will amplify the event and will have no impact on its propagation speed. In contrast, if they are in quadrature ($\phi_v = \pi/2$) the meridional advection will propagate westward without any effect on its growth. An in-between phase shift leads to both amplification and propagation. The same effect is obtained for the vertical velocity. The diagnostic algorithm developed for estimating the phase shifts at each vertical level determines the times at which the v^* and w^* composites cross the zero value.[3] Figure 13a displays the vertical profiles of the phase differences ϕ_v and ϕ_w up to 250 hPa. It confirms the vertical structure of the composite provided by Fig. 9a, with a phase shift ϕ_v of about 60° at the surface for v^* ahead of the moist event and about 0° at the AEJ level (600 hPa). Above, the phase shift increases slightly. The vertical velocity is in phase opposition with q^* below 600 hPa (see Fig. 9b). Above 600 hPa, the vertical motion is almost in phase ($\phi_w \approx 30°$) with the wet event. The impact of such phase shifts on the propagation (Fig. 13b) and growth (Fig. 13c) are detailed below.

The mean zonal wind explains the propagation of the event around the AEJ level. Below, the westward propagation mainly results from the phase shift ϕ_v. In contrast, the vertical velocity has little impact on the propagation of the mode. Globally, this simple linear model explains the first-order propagation of moist anomalies although with some overestimation (4 m s^{-1}) at midlevels and underestimation (-2 m s^{-1}) at low levels.

Figure 13c shows three profiles of PW* growth rates computed in different ways as discussed above. First, the estimation of the growth rate of q^* at each vertical level (dotted line) fluctuates weakly between 0.1 and 0.25 (at the upper and lower levels, respectively) and is consistent with the bulk observed growth rate of PW* of about 0.2 day^{-1}, which appears close to previous findings in AEW studies [see Table 1 in Hall et al. (2006)]. The growth rate given by the linear adiabatic analysis fails to capture the observed growth rate in the 875–600-hPa layer. In fact, below 600 hPa, w^* has a dramatic damping effect on the wave because of the phase opposition; that is, during the wet (dry) event, the low-level subsidence (ascent) efficiently dries (moistens) the atmosphere. The meridional advection, positive phase shift ϕ_v of which contributes to the mode growths, is insufficient to counter the effects of the vertical circulation. Above 600 hPa, both vertical ascent and meridional advection help to amplify the event so that the linear model overestimates the growth rate (0.3–0.5 day^{-1}) as compared with observations. So, the above simple linear and

[3] This is more precise than using extremum values.

adiabatic diagnostic analysis explains the propagation of PW* anomalies to the first order at all heights. Regarding their amplification, there is a need for a moisture source under 600 hPa and a moisture sink above. Convective diabatic processes are good candidates. Condensation in the upper troposphere will dry and thus damp down the growth of moisture anomalies, whereas evaporation of precipitation and convective eddies below 600 hPa will act as a moisture source, able to balance the damping effect of the vertical circulation. This interpretation is supported by previous analyses of the convective impact on the apparent moisture sink Q_2 (Yanai et al. 1973; Johnson 1984). Specific observational and numerical studies dedicated to West Africa, where severe dry conditions prevail (Leary and Houze 1980; Chong and Hauser 1989; Lafore et al. 1988; Caniaux et al. 1994), have emphasized the moistening role of convective eddies and rain evaporation, more specifically below trailing stratiform parts of convective systems. Further analysis of these diabatic contributions will be developed in a forthcoming paper.

This linear and adiabatic model has been applied at different locations in the Sahel band, confirming the above conclusions. Nevertheless, the results (not shown) for box B4 (coastal region) indicate a weaker phase difference ϕ_v between specific humidity and meridional wind (30° instead of 60°) than for B3 below 700 hPa. As a result, the growth rate due to meridional wind increases while the propagation velocity decreases, so our linear and adiabatic growth rate fits the observed one better in that coastal region. Diabatic effects are thus less preponderant. On the one hand, although mean surface evaporation is higher there, its contribution remains small at the AEW time scale as over B3. On the other hand, the low-level atmosphere is becoming moister at the coast, so rain evaporation should play a weaker role in the growth of PW anomalies. Furthermore, over the Atlantic Ocean, ϕ_v (and baroclinicity) becomes much weaker, leading to a decreasing propagation velocity, which is consistent with the findings of Reed et al. (1977) and Kiladis et al. (2006).

7. Conclusions

Variables associated directly with convection (e.g., precipitation, OLR) are often too complex to disentangle the processes involved in its spatial and temporal variability. There is a need to deal with simpler, intermediate variables, whose dynamics are easier to tackle and whose relationship with convection is more direct. Precipitable water can be seen as one of these variables, useful to investigate the West African monsoon (WAM) intraseasonal variability.

PW intraseasonal variability has been documented with a long series of data provided by ERA-Interim, and validated against ground-based GPS retrievals. The study of the summer-season climatology reveals a large meridional gradient of PW in the Sahel band, collocated with a maximum of PW variance. The contribution of the intraseasonal scale to the total variability is assessed to be about 55% in the western Sahel. There, ISV is dominated by synoptic fluctuations (1–10 days) while the eastern Sahel is dominated by longer time scales (10–90 days). This study thus provides a focus on the western Sahel synoptic variability (i.e., on AEWs). To assess the variability of PW at the synoptic scale, a composite analysis highlights a moist perspective of African easterly waves, with westward-propagating wet and dry anomalies. Such synoptic dry and wet events are frequent (4–5 month^{-1}) and robust. Thus the monitoring and forecasting of PW at short to medium ranges can provide useful information for early warning systems. These structures are driven by a particular coupling between the mid- and low-level circulations associated with AEWs. These events are concomitant with large rainfall anomalies (~30% of the seasonal mean at t_0) spatially consistent with previous studies. The ERA-Interim, although consistent overall with satellite-derived precipitation, experiences difficulties in capturing the phase shift between precipitation and PW maximum (the PW maximum follows the rainfall maximum). As humidity is one of the limiting factors for rainfall, we also argue that PW anomalies are a relevant diagnostic of strong AEW and of the related convective activity along the northern side of the AEJ.

A moisture budget has been proposed to gain further insight into the PW signature of AEW dynamics. Vertical advection is found to be the precursor of the anomaly growth through low-level convection, followed by horizontal advection dominated by its meridional component.

A linear and adiabatic approach to the PW equation provides realistic propagation properties of the anomalies once they have been generated. The growth rate computed from the phase shift between meridional and vertical wind versus PW underestimates (overestimates) the growth rate derived from the composite, especially in the 850–650-hPa (500–300-hPa) layer, where diabatic processes such as evaporation (condensation) and nonlinearity are probably critical. In fact, the dryness of the mean state at 850–650 hPa may well support large humidification through rainfall evaporation and thus amplify the anomalies. At the same time, upper-level overestimated growth can also be explained by the fact that condensation processes, which represent a humidity sink, are neglected. Although basic, the adiabatic

analysis points out the role of both dynamic and physical processes for a growing and propagative humidity wave induced by an AEW. A future part of this work will focus on the vertical profiles of the budget of both moisture and temperature to propose a complete description and understanding of dynamic and diabatic processes.

Acknowledgments. The authors are grateful to the anonymous reviewers for their thoughtful and useful comments on the original manuscript. We also thank Florence Favot for her assistance in computing facilities. ERA-Interim data were provided by the ECMWF. The 1DD GPCP data were provided by the NASA/Goddard Space Flight Center's Laboratory for Atmospheres, which develops and computes the 1DD as a contribution to the GEWEX Global Precipitation Climatology Project. The interpolated OLR dataset was provided by NOAA-ESRL PSD, Boulder, Colorado, from their website at http://www.esrl.noaa.gov/psd/. The authors thank O. Bock and M. N. Bouin, IGN, for having processed the GPS data and E. Doerflinger, CNRS, and national meteorological services from the different countries hosting GPS receivers for having participated to the installation and maintenance of the AMMA GPS network. The present work was supported by Météo-France.

REFERENCES

Barthe, C., N. Asencio, J.-P. Lafore, M. Chong, B. Campistron, and F. Cazenave, 2010: Multi-scale analysis of the 25–27 July 2006 convective period over Niamey: Comparison between Doppler radar observations and simulations. *Quart. J. Roy. Meteor. Soc.,* **136** (Suppl.), 190–208.

Bock, O., and M. Nuret, 2009: Verification of NWP model analyses and radiosonde humidity data with GPS precipitable water vapor estimates during AMMA. *Wea. Forecasting,* **24,** 1085–1101.

——, and Coauthors, 2008: West African Monsoon observed with ground-based GPS receivers during African Monsoon Multidisciplinary Analysis (AMMA). *J. Geophys. Res.,* **113,** D21105, doi:10.1029/2008JD010327.

Bretherton, C. S., M. E. Peters, and L. E. Back, 2004: Relationships between water vapor path and precipitation over the tropical oceans. *J. Climate,* **17,** 1517–1528.

Brown, R. G., and C. D. Zhang, 1997: Variability of midtropospheric moisture and its effect on cloud-top height distribution during TOGA COARE. *J. Atmos. Sci.,* **54,** 2760–2774.

Cadet, D. L., and S. H. Houston, 1984: Precipitable water over West Africa and the Eastern/Central Atlantic Ocean during summer 1979. *J. Meteor. Soc. Japan,* **62,** 761–774.

——, and N. O. Nnoli, 1987: Water vapour transport over Africa and the Atlantic Ocean during summer 1979. *Quart. J. Roy. Meteor. Soc.,* **113,** 581–602.

Caniaux, G., J.-L. Redelsperger, and J.-P. Lafore, 1994: A numerical study of the stratiform region of a fast-moving squall line. Part I: General description and water and heat budgets. *J. Atmos. Sci.,* **51,** 2046–2074.

Chong, M., and D. Hauser, 1989: A tropical squall line observed during the COPT 81 experiment in West Africa. Part II: Water budget. *Mon. Wea. Rev.,* **117,** 728–744.

Cornforth, R. J., B. J. Hoskins, and C. D. Thorncroft, 2009: The impact of moist processes on the African easterly jet–African easterly wave system. *Quart. J. Roy. Meteor. Soc.,* **135,** 894–913.

Couvreux, F., F. Guichard, O. Bock, B. Campistron, J.-P. Lafore, and J.-L. Redelsperger, 2010: Synoptic variability of the monsoon flux over West Africa prior to the onset. *Quart. J. Roy. Meteor. Soc.,* **136** (Suppl.), 160–174.

Diongue, A., J.-P. Lafore, J.-L. Redelsperger, and R. Roca, 2002: Numerical study of a Sahelian synoptic weather system: Initiation and mature stages of convection and its interactions with the large-scale dynamics. *Quart. J. Roy. Meteor. Soc.,* **128,** 1899–1928.

Duchon, C. E., 1979: Lanczos filtering in one and two dimensions. *J. Appl. Meteor.,* **18,** 1016–1022.

Fink, A., and A. Reiner, 2003: Spatiotemporal variability of the relation between African easterly waves and West African squall lines in 1998 and 1999. *J. Geophys. Res.,* **108,** 4332, doi:10.1029/2002JD002816.

Hall, N. M. J., G. N. Kiladis, and C. D. Thorncroft, 2006: Three-dimensional structure and dynamics of African easterly waves. Part II: Dynamical modes. *J. Atmos. Sci.,* **63,** 2231–2245.

Holloway, C. E., and J. D. B. Neelin, 2010: Temporal relations of column water vapor and tropical precipitation. *J. Atmos. Sci.,* **67,** 1091–1105.

Huffman, G. J., R. F. Adler, M. M. Morrissey, D. T. Bolvin, S. Curtis, R. Joyce, B. McGavock, and J. Susskind, 2001: Global precipitation at one degree daily resolution from multisatellite observations. *J. Hydrometeor.,* **2,** 36–50.

Janicot, S., and Coauthors, 2008: Large-scale overview of the summer monsoon over West Africa during the AMMA field experiment in 2006. *Ann. Geophys.,* **26,** 2569–2595.

——, F. Mounier, N. M. J. Hall, S. Leroux, B. Sultan, and G. N. Kiladis, 2009: The West African monsoon dynamics. Part IV: Analysis of the 25–90-day variability of convection and the role of the Indian monsoon. *J. Climate,* **22,** 1541–1565.

——, ——, S. Gervois, S. Benjamin, and G. N. Kiladis, 2010: The dynamics of the West African monsoon. Part V: The detection and role of the dominant modes of convectively coupled equatorial Rossby waves. *J. Climate,* **23,** 4005–4024.

——, and Coauthors, 2011: Intraseasonal variability of the West African monsoon. *Atmos. Sci. Lett.,* **12,** 58–66.

Johnson, R. H., 1984: Partitioning tropical heat and moisture budgets into cumulus and mesoscale components: Implications for cumulus parameterization. *Mon. Wea. Rev.,* **112,** 1590–1601.

Kanamitsu, M., W. Ebisuzaki, J. Woollen, S.-K. Yang, J. J. Hnilo, M. Fiorino, and G. L. Potter, 2002: NCEP–DOE AMIP-II Reanalysis (R-2). *Bull. Amer. Meteor. Soc.,* **83,** 1631–1643.

Kiladis, G. N., C. D. Thorncroft, and N. M. J. Hall, 2006: Three-dimensional structure and dynamics of African easterly waves. Part I: Observations. *J. Atmos. Sci.,* **63,** 2212–2230.

Lafore, J.-P., and M. W. Moncrieff, 1989: A numerical investigation of the organization and interaction of the convective and stratiform regions of tropical squall lines. *J. Atmos. Sci.,* **46,** 521–544.

——, J.-L. Redelsperger, and G. Jaubert, 1988: Comparison between a three-dimensional simulation and Doppler radar data of a tropical squall line: Transports of mass, momentum, heat, and moisture. *J. Atmos. Sci.,* **45,** 3483–3500.

Leary, C. A., and R. A. Houze, 1980: The contribution of mesoscale motions to the mass and heat fluxes of an intense tropical convective system. *J. Atmos. Sci.,* **37,** 784–796.

Liebmann, B., and C. A. Smith, 1996: Description of a complete (interpolated) outgoing longwave radiation dataset. *Bull. Amer. Meteor. Soc.,* **77,** 1275–1277.

Lothon, M., B. Campistron, M. Chong, F. Couvreux, F. Guichard, C. Rio, and E. Williams, 2011: Life cycle of a mesoscale circular gust front observed by a C-band Doppler radar in West Africa. *Mon. Wea. Rev.,* **139,** 1370–1388.

Mapes, B. E., R. Milliff, and J. Morzel, 2009: Composite life cycle of maritime tropical mesoscale convective systems in scatterometer and microwave satellite observations. *J. Atmos. Sci.,* **66,** 199–208.

Matthews, A. J., 2004: Intraseasonal variability over tropical Africa during northern summer. *J. Climate,* **17,** 2427–2440.

Mounier, F., and S. Janicot, 2004: Evidence of two independent modes of convection at intraseasonal timescale in the West African summer monsoon. *Geophys. Res. Lett.,* **31,** L16116, doi:10.1029/2004GL020665.

——, ——, and G. N. Kiladis, 2008: The West African monsoon dynamics. Part III: The quasi-biweekly zonal dipole. *J. Climate,* **21,** 1911–1928.

Neelin, J., O. Peters, and K. Hales, 2009: The transition to strong convection. *J. Atmos. Sci.,* **66,** 2367–2384.

Parsons, D. B., J.-L. Redelsperger, and K. Yoneyama, 2000: The evolution of the tropical Western Pacific atmosphere–ocean system following the arrival of a dry intrusion. *Quart. J. Roy. Meteor. Soc.,* **126,** 517–548.

Redelsperger, J.-L., A. Diongue, A. Diedhiou, J.-P. Ceron, M. Diop, J.-F. Gueremy, and J.-P. Lafore, 2002: Multi-scale description of a Sahelian synoptic weather system representative of the West African Monsoon. *Quart. J. Roy. Meteor. Soc.,* **128,** 1229–1257.

Reed, R. J., D. C. Norquist, and E. E. Recker, 1977: The structure and properties of African wave disturbances as observed during Phase III of GATE. *Mon. Wea. Rev.,* **105,** 317–333.

Roca, R., R. Guzman, J. Lemond, J. Meijers, L. Picon, and H. Brogniez, 2011: Tropical and extra-tropical influences on the distribution of free tropospheric humidity over the intertropical belt. *Surv. Geophys.,* **33,** 565–583.

Roehrig, R., F. Chauvin, and J.-P. Lafore, 2011: 10–25-day intraseasonal variability of convection over the Sahel: A role of the Saharan heat low and midlatitudes. *J. Climate,* **24,** 5863–5878.

Schwendike, J., and S. C. Jones, 2010: Convection in an African Easterly Wave over West Africa and the eastern Atlantic: A model case study of *Helene* (2006). *Quart. J. Roy. Meteor. Soc.,* **136** (Suppl.), 364–396.

Sherwood, S. C., 1999: Convective precursors and predictability in the tropical western Pacific. *Mon. Wea. Rev.,* **127,** 2977–2991.

——, P. Minnis, and M. McGill, 2004: Deep convective cloud-top heights and their thermodynamic control during CRYSTAL-FACE. *J. Geophys. Res.,* **109,** D20119, doi:10.1029/2004JD004811.

Simmons, A., S. Uppala, D. Dee, and S. Kobayashi, 2007: ERA-Interim: New ECMWF reanalysis products from 1989 onwards. *ECMWF Newsletter,* No. 110, ECMWF, Reading, United Kingdom, 26–35.

Smull, B. F., and R. A. Houze Jr., 1987: Rear inflow in squall lines with trailing stratiform precipitation. *Mon. Wea. Rev.,* **115,** 2869–2889.

Sultan, B., C. Baron, M. Dingkuhn, and S. Janicot, 2005: Agricultural impacts of large-scale variability of the West African monsoon. *Agric. For. Meteor.,* **128,** 93–110.

Thorncroft, C. D., and B. J. Hoskins, 1994: An idealized study of African easterly waves. II: A nonlinear view. *Quart. J. Roy. Meteor. Soc.,* **120,** 983–1015.

——, and M. Blackburn, 1999: Maintenance of the African easterly jet. *Quart. J. Roy. Meteor. Soc.,* **125,** 763–786.

Yanai, M., S. Esbensen, and J. H. Chu, 1973: Determination of bulk properties of tropical cloud clusters from large-scale heat and moisture budgets. *J. Atmos. Sci.,* **30,** 611–627.

Zelinka, M. D., and D. L. Hartmann, 2009: Response of humidity and clouds to tropical deep convection. *J. Climate,* **22,** 2389–2404.